Chapter 6

Measurement of production cross section for WW via DPS and effective cross section parameter

In previous Chapter, measurement of production cross section for same-sign WW via DPS processes using same-sign WW events based on the electron-muon final state has been presented. This Chapter includes the same studies performed using the dimuon final state along with a combination of results based on the two final states [1]. The major part of this Chapter is dedicated to the outline of the analysis with dimuon final state, followed by a detailed description of the combined studies. The event selection criteria and background estimation techniques are identical for the two final states. Both the final states rely on a multivariate analysis to discriminate between the signal and background processes.

6.1 Signal and Background Processes

The signal process includes the decay of two W bosons into a pair of muons in association with $p_{\mathrm{T}}^{\mathrm{miss}}$ coming from the neutrinos. Same set of signal and background

samples as listed in Table 5.1 is used for the current analysis. The dimuon final state benefits from the negligible charge misidentification probability and good momentum resolution for the muons at the CMS detector [2]. Due to this reason, the background contributions are somewhat different for the two final states and these differences are mentioned here.

Events from the DY processes contribute as background when $p_{\mathrm{T}}^{\mathrm{miss}}$ is observed due to mismeasurement of the lepton momenta or mismeasurement of the hadronic recoil activity. In case of same-sign leptons in the final state, events from the DY processes can also arise when charge of one of the leptons is misreconstructed. Due to negligible charge misidentification probability for the muons, the dimuon final state is less contaminated from the DY production and decays of top quark-antiquark pairs. Furthermore, no background contributions are expected from the Wγ and fully leptonic decay of $\mathrm{t\bar{t}}$ production processes for the dimuon final states. The W+jets and QCD multijet production processes can mimic the signal process, when one or both the final state leptons are misidentified. As discussed in Chapter 5, the W+jets and QCD multijet production processes respectively fall under the category of *prompt-misid.* and *misid.-misid.* events.

6.2 Event Selection

The DoubleMu (DoubleMuon) primary datasets collected during pp collisions at $\sqrt{\mathrm{s}} = 8\,\mathrm{TeV}$, corresponding to an integrated luminosity of $19.7\,\mathrm{fb}^{-1}$, are used to perform current studies. During this data taking period in the year 2012, the instantaneous luminosity varied over the range 10^{29}–$10^{33}\,\mathrm{cm}^{2}\mathrm{s}^{-1}$. The trigger used to select the dimuon events requires the presence of at least two muons with the leading (subleading) muon $p_{\mathrm{T}} > 17(8)\,\mathrm{GeV}$. The dimuon trigger is found to have an efficiency of 90% with respect to the offline muon selection criteria. The muon, $p_{\mathrm{T}}^{\mathrm{miss}}$, and PV selection criteria are essentially the same as described in Section 5.6.

Table 6.1: Same-sign WW event selection criteria used for the dimuon final state.

Pair of same-sign muons
Leading muon $p_{\mathrm{T}} > 20\,\mathrm{GeV}$ and subleading muon $p_{\mathrm{T}} > 10\,\mathrm{GeV}$
Not more than two isolated and identified muons with $p_{\mathrm{T}} > 10\,\mathrm{GeV}$
$p_{\mathrm{T}}^{\mathrm{miss}} > 20\,\mathrm{GeV}$
$\mathrm{m}_{\mu\mu} > 20\,\mathrm{GeV}$ and $\mathrm{m}_{\mu\mu} \notin [75{,}105]\,\mathrm{GeV}$
$\lvert\vec{p}_{\mathrm{T}_{\mu_1}}\rvert + \lvert\vec{p}_{\mathrm{T}_{\mu_2}}\rvert > 45\,\mathrm{GeV}$

The muon candidates are required to be geometrically isolated from other charged particles and energy deposits, using the analogous procedure as described in Section 4.5. The same-sign WW selection criteria used for the dimuon final state are listed in Table 6.1. The offline selection criteria demand the presence of exactly two same-sign well identified and isolated muons. The leading (subleading) muon is required to have p_{T} greater than 20 (10) GeV to match the trigger requirement. The muons are required to lie within a geometrical region defined by $|\eta| < 2.4$. To reduce background contributions from the ZZ, WZ, and Wγ^* production processes where the final state can have more than two muons, events having three or more well reconstructed muons with $p_{\mathrm{T}} > 10\,\mathrm{GeV}$ are rejected. Furthermore, to reduce events from low-mass resonances, the two selected muons are required to have a dimuon invariant mass ($\mathrm{m}_{\mu\mu}$) greater than 20 GeV. To minimize background contributions from the DY production processes, $\mathrm{m}_{\mu\mu}$ is required to be away from the Z boson mass peak ($\mathrm{m}_{\mu\mu} \notin [75, 105]\,\mathrm{GeV}$) and $p_{\mathrm{T}}^{\mathrm{miss}}$ is needed to be greater than 20 GeV. A minimum threshold of 45 GeV on the scalar sum of the p_{T} of the two muons is also enforced to reduce background contributions from the QCD multijet events.

6.3 Background Estimation Techniques

The background contributions from the *prompt-misid.* and *misid.-misid.* processes are estimated using the same procedure as described in Section 5.7.1. However, the selection criteria used to construct the misidentified lepton enriched region is slightly different from the one used for the electron-muon final state (Table 5.4). The definition of the misidentified lepton enriched region depends on the distinct signatures of the background processes which are estimated using this method. For the dimuon final state, the major background contribution is expected from the QCD multijet process. Hence, the misidentified lepton enriched region is constructed such that it is dominated by QCD multijet events. The selection criteria used to construct misidentified muon enriched region is given in Table 6.2.

Table 6.2: Selection criteria used to construct misidentified muon enriched region in the data.

Only one loose muon with $p_{\mathrm{T}} > 10\,\mathrm{GeV}$
$p_{\mathrm{T}}^{\mathrm{miss}} < 20\,\mathrm{GeV}$
$\mathrm{m}_{\mathrm{T}}(\mu, p_{\mathrm{T}}^{\mathrm{miss}}) < 20\,\mathrm{GeV}$

The misidentified muon enriched event sample is defined in the data with the requirement of only one loosely identified muon to reduce the contributions from the sources of prompt muons. The *loose selection* criteria require the muons with $p_{\mathrm{T}} > 10\,\mathrm{GeV}$ and isolation variable < 0.4. The ratio of the number of muons passing the analysis level selection (tight selection) to the ones passing the *loose selection* criteria in the misidentified muon enriched sample is termed as the muon misidentification rate. While calculating the muon misidentification rate, the contributions from DY and W+jets processes are also subtracted (EWK subtraction) to avoid any

Table 6.3: Muon misidentification rate as a function of muon p_{T} and η.

p_{T}[GeV]	$0 < \lvert\eta\rvert < 1$	$1 < \lvert\eta\rvert < 1.4$	$1.4 < \lvert\eta\rvert < 2$	$2 < \lvert\eta\rvert < 2.4$
$10 < p_{\mathrm{T}} < 15$	0.291±0.003	0.319±0.004	0.355±0.005	0.369±0.007
$15 < p_{\mathrm{T}} < 20$	0.232±0.003	0.264±0.005	0.295±0.006	0.318±0.009
$20 < p_{\mathrm{T}} < 25$	0.216±0.005	0.241±0.009	0.277±0.010	0.302±0.015
$25 < p_{\mathrm{T}} < 35$	0.207±0.010	0.249±0.017	0.281±0.019	0.304±0.030
$p_{\mathrm{T}} > 35$	0.204±0.020	0.234±0.033	0.281±0.034	0.274±0.054

Table 6.4: Selection criteria for prompt muon enriched sample.

Only two opposite sign well identified muons
Leading muon $p_{\mathrm{T}} > 20\,\mathrm{GeV}$ and subleading muon $p_{\mathrm{T}} > 10\,\mathrm{GeV}$
$70 < \mathrm{m}_{\mu\mu} < 110\,\mathrm{GeV}$

contamination from the prompt muons. Table 6.3 shows the extracted values of muon misidentification rate (∼20–35%) as a function of muon kinematic variables after applying the EWK subtraction. Only statistical uncertainties on these numbers are given here. The systematic uncertainties are discussed further in Section 6.4.

This background estimation technique also uses muon prompt ratios which are extracted using a data control sample enriched in Z boson events referred to as the prompt muon enriched region (Table 6.4). The use of prompt ratios is to take into account the real/prompt lepton contamination in the misidentified muon enriched event sample. The muon prompt ratio is defined as the number of muons passing the

Table 6.5: Muon prompt ratios as a function of its p_{T} and η. Only statistical uncertainties on these values are mentioned here.

p_{T} [GeV]	$0 < \eta < 1.4$	$1.4 < \eta < 2.4$
$10 < p_{\mathrm{T}} < 15$	0.70±0.01	0.75±0.01
$15 < p_{\mathrm{T}} < 20$	0.757±0.008	0.81±0.01
$20 < p_{\mathrm{T}} < 25$	0.806±0.006	0.86±0.01
$25 < p_{\mathrm{T}} < 35$	0.899±0.003	0.929±0.005
$p_{\mathrm{T}} > 35$	0.97±0.01	0.97±0.02

tight selection criteria to the number of muons passing the *loose selection* criteria in the prompt muon enriched sample. Table 6.5 summarizes the muon prompt ratios obtained as a function of muon p_{T} and η. In an ideal case, lepton prompt ratios should be close to 1, however deviations are observed due to the detector inefficiencies.

After the evaluation of muon misidentification and prompt ratios, event yields for *misid.-misid.* and *prompt-misid.* backgrounds are estimated using the formulas given in Section 5.7.1.1. A extrapolation factor is defined in terms of the muon misidentification rate and muon prompt ratios. This factor relates the contributions from the misidentified background events accumulated with this criteria to the ones obtained after passing the same-sign WW selection criteria. These backgrounds make up the major part of the background events for this final state (∼70%). The contributions from the Wγ^* background processes are estimated in the similar manner as described in Section 5.7.3. The systematic uncertainties arising due to these background estimation procedures are described in the following Section.

6.4 Systematic Uncertainties

Systematic uncertainties in this analysis arise from following sources:

- **Luminosity calibration:** The uncertainty on the luminosity estimation of 2.6% is directly translated into an uncertainty on the yields for both signal and background simulated samples [3].

- **MC pileup reweighting:** MC simulated samples are reweighted according to the observed pileup distribution in the data. This reweighting procedure has an uncertainty of 4.5% [3], which is added to all the MC simulated samples.

- **Muon reconstruction and identification:** The uncertainty due to different muon reconstruction and identification efficiencies for the data and MC simulated samples is found to contribute less than 1% [4] for all the MC simulated samples. This also includes the effect of uncertainty on the scale factor used to account for different trigger efficiencies in the data and MC simulated samples.

- $p_{\mathrm{T}}^{\mathrm{miss}}$ **modelling:** $p_{\mathrm{T}}^{\mathrm{miss}}$ measurement is affected by the possible mismeasurement of leptons, jets, as well as the additional contributions from the pileup interactions. The lepton momentum scale, jet energy scale, and scales of the unclustered PF candidates are varied within their respective uncertainties and the effect is then propagated to $p_{\mathrm{T}}^{\mathrm{miss}}$. This uncertainty affects the signal yield by $< 1\%$ and various background processes by 1–4%.

- **Data-driven estimation of background processes:** This is the major source of systematic uncertainty affecting the current measurement. As discussed in Section 5.7.1.2, these uncertainties arise from the p_{T} and flavor of the jet being misidentified as a muon. The uncertainty due to p_{T} of the jet, or more accurately of the partons, is considered to account for the possible differences between the reconstructed jet energy, and the reconstructed energy

of the misidentified lepton. A jet with a given energy can be misidentified as a lepton with different energy. In general, the rate at which jets are misidentified as leptons depends on both the energy of the initial jet and the energy of the lepton being misidentified. Also, the efficiency of the selection cut on the lepton isolation variable depends on the p_{T} of the lepton candidate. To account for this source of systematic uncertainty, we calculate the muon misidentification rate by requiring at least one jet with $p_{\mathrm{T}} > 25\,\mathrm{GeV}$ in addition to selection criteria given in Table 6.2. To gain a reasonable knowledge on the upper and lower bounds on this used jet p_{T} threshold, the distribution of the muon isolation variable in the misidentified muon enriched control sample is compared with the muons in QCD multijet simulated sample. This spectrum is a representative of the p_{T} spectrum of a particular parton which produces the misidentified lepton after fragmentation and hadronization. The cut value on the jet p_{T} that makes these distributions comparable is used to calculate the effect of this systematic uncertainty. Figure 6.1 shows the comparison of the isolation variable distribution for the muons in the misidentified muon enriched sample with and without any cut on the jet p_{T}, QCD multijet MC simulated sample, and the signal phase space region i.e. at the level of same-sign WW selection but with the tight muons having isolation variable < 0.4. Here, it is clear that the request of a minimum jet p_{T} threshold changes the isolation spectrum behavior of the muons in the signal region and misidentified muon control region (CR). The muon misidentification rates change by 10% after requiring a jet with $p_{\mathrm{T}} > 25\,\mathrm{GeV}$ with respect to the ones extracted using the selection criteria given in Table 6.2.

The second source of systematic uncertainty arises due to the different flavors of misidentified jets: quark jets, gluon jets, and heavy flavor jets etc. Each of these different jet flavors can have a different misidentification rate. As explained before, the muon misidentification rate is measured in a control sample enriched with QCD multijet events which are dominated by gluon

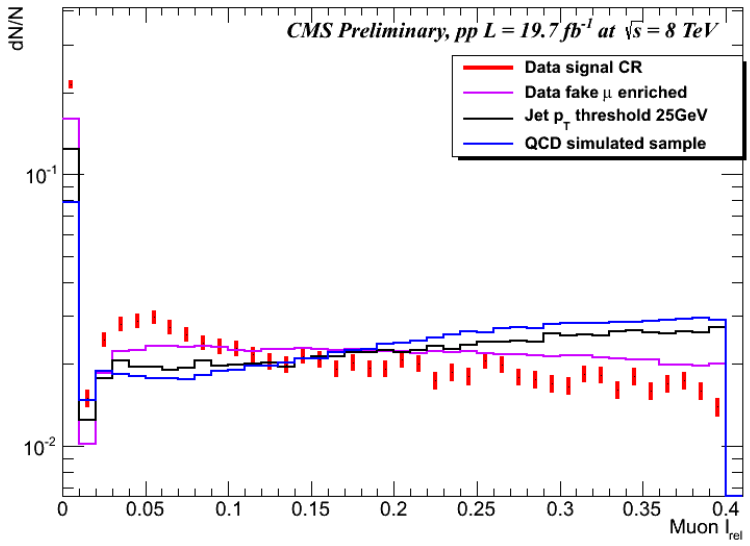

Figure 6.1: Isolation variable spectra for the muons in different phase space regions.

jets. The muon misidentification rate so obtained is used to estimate the contributions from the W+jets background, which tend to have quark-initiated jets.

In order to extract quantitative measure of the systematic uncertainties due different jet flavors, we perform a closure test on the W+jets MC simulated sample by comparing the background yields predicted by the MC simulation sample with those extracted using this data-driven method. To be consistent, the muon misidentification rate is calculated using the QCD multijet simulated sample and then applied to the *tight-fail* sample selected in the W+jets MC simulated sample. The degree of disagreement yields a quantitative measure of the systematic uncertainty. These two sources of systematic uncertainty are added in quadrature to give a total systematic uncertainty of 40% for each of the *misid.-misid.* and *prompt-misid.* events yields. These uncertainties also include the effect of statistical uncertainties on the muon misidentification rate and muon prompt ratios.

- **Theoretical uncertainty:** The effect of variations in PDFs, the value of α_s, and missing higher-order corrections on the cross section for various simulated processes are also included. For the Wγ^* background process, 30% uncertainty is obtained on its normalization [3].

6.5 Data-MC Validation

After applying the same-sign WW selection criteria (Table 6.1), the distributions of the kinematic observables are compared for the signal and various background processes with the data. Figures [6.2-6.4] show the distributions of the kinematic observables at the detector level. The contributions of *misid.-misid.* and *prompt-misid.* backgrounds are estimated from the data, while rest of the backgrounds are taken from the MC simulations. Overall agreement between the data, predicted signal, and background yields is within statistical and systematic uncertainties.

‘

6.6 Multivariate Analysis

A multivariate analysis based on BDTs is performed to increase the signal sensitivity as compared to a single observable. BDTs are trained using the simulated signal sample, while a background ensemble is constructed by mixing the major background processes (*misid.-misid.*, *prompt-misid.*, and WZ). Following set of kinematic observables are used to train BDTs:

- p_{T} of the leading and subleading muons, p_{T_1}, p_{T_2};
- $p_{\mathrm{T}}^{\mathrm{miss}}$;
- azimuthal angular separation between the leading/subleading muon and $\vec{p}_{\mathrm{T}}^{\,\mathrm{miss}}$, $\Delta\phi(\vec{p}_{\mathrm{T}_1}, \vec{p}_{\mathrm{T}}^{\,\mathrm{miss}})$ and $\Delta\phi(\vec{p}_{\mathrm{T}_2}, \vec{p}_{\mathrm{T}}^{\,\mathrm{miss}})$;

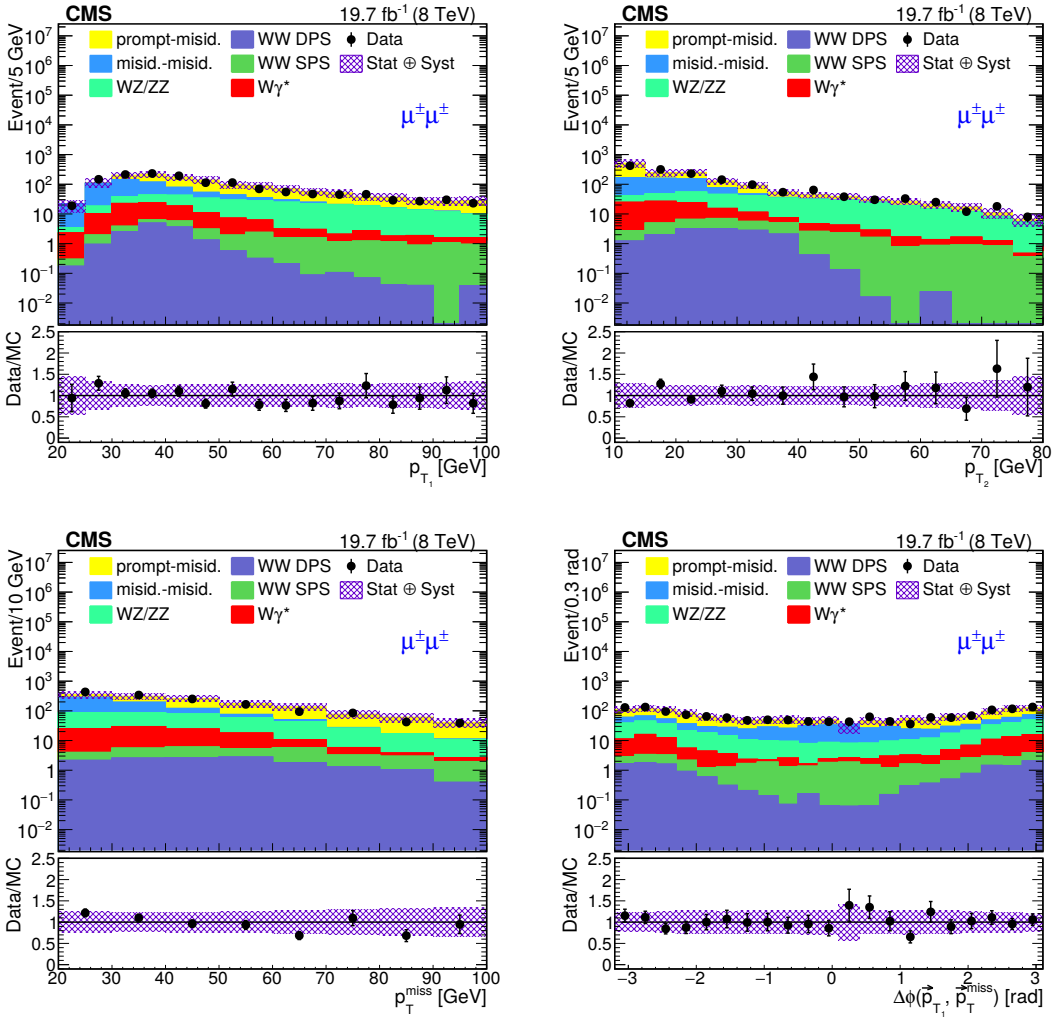

Figure 6.2: The distributions of the observables sensitive to DPS in the dimuon channel: p_{T_1} (top left), p_{T_2} (top right), $p_{\mathrm{T}}^{\mathrm{miss}}$ (bottom left), and $\Delta\phi(\vec{p}_{\mathrm{T}_1}, \vec{p}_{\mathrm{T}}^{\,\mathrm{miss}})$ (bottom right). The data are represented using the black dots and the shaded histograms represent the predicted signal and background processes normalized according to the theoretical cross sections and the luminosity. For each individual distribution, the ratio of the number of events observed in the data to that predicted by the simulation, along with the associated statistical uncertainty is also shown. The hatched bands in all cases represent the sum of the systematic and statistical uncertainties on the simulation, added in quadrature.

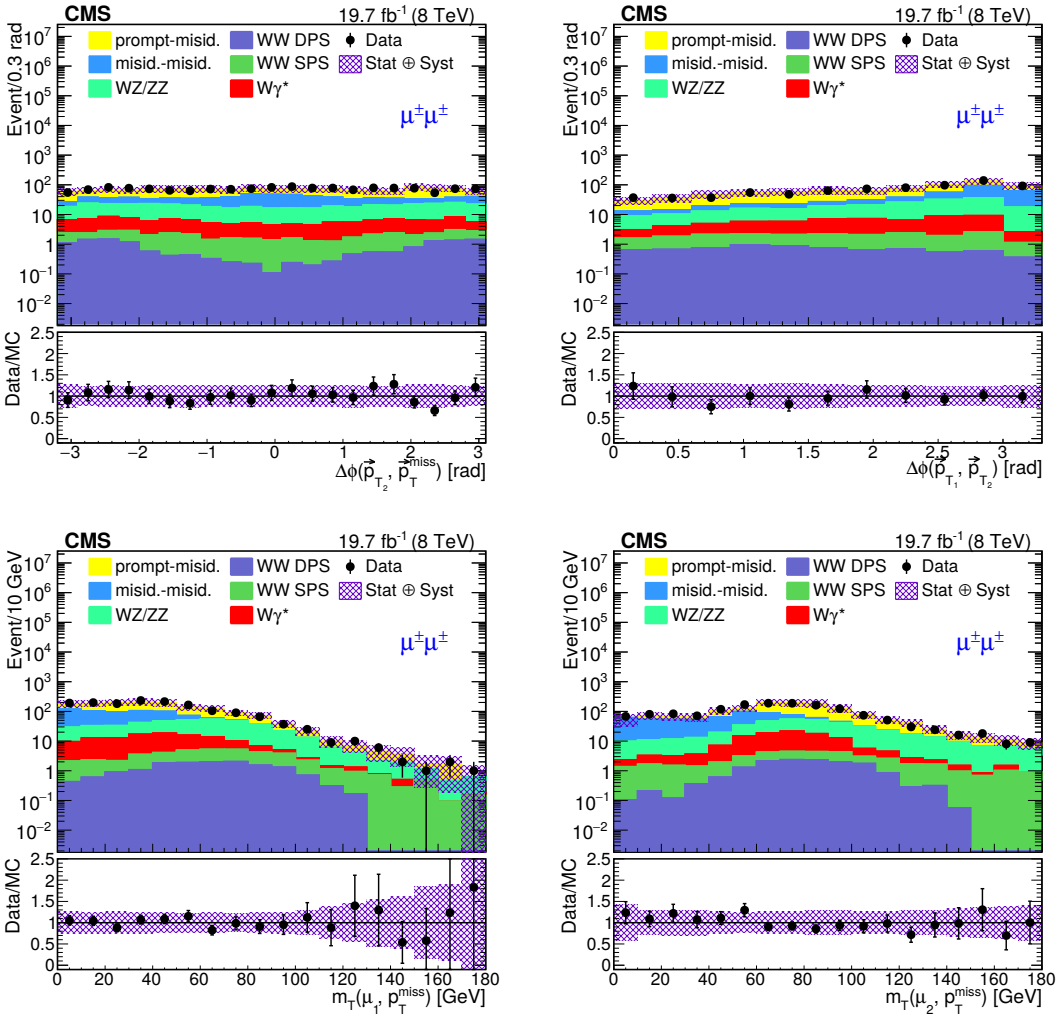

Figure 6.3: DPS sensitive observables in the dimuon channel: $\Delta\phi(\vec{p}_{\mathrm{T}_2}, \vec{p}_{\mathrm{T}}^{\,\mathrm{miss}})$ (top left), $\Delta\phi(\vec{p}_{\mathrm{T}_1}, \vec{p}_{\mathrm{T}_2})$ (top right), $\mathrm{m_T}(\mu_1, \vec{p}_{\mathrm{T}}^{\,\mathrm{miss}})$ (bottom left), and $\mathrm{m_T}(\mu_2, \vec{p}_{\mathrm{T}}^{\,\mathrm{miss}})$ (bottom right). The data are represented using the black dots and the shaded histograms represent the predicted signal and background processes normalized according to the theoretical cross sections and the luminosity. For each individual distribution, the ratio of the number of events observed in the data to that predicted by the simulation, along with the associated statistical uncertainty is also shown. The hatched bands in all cases represent the sum of the systematic and statistical uncertainties on the simulation, added in quadrature.

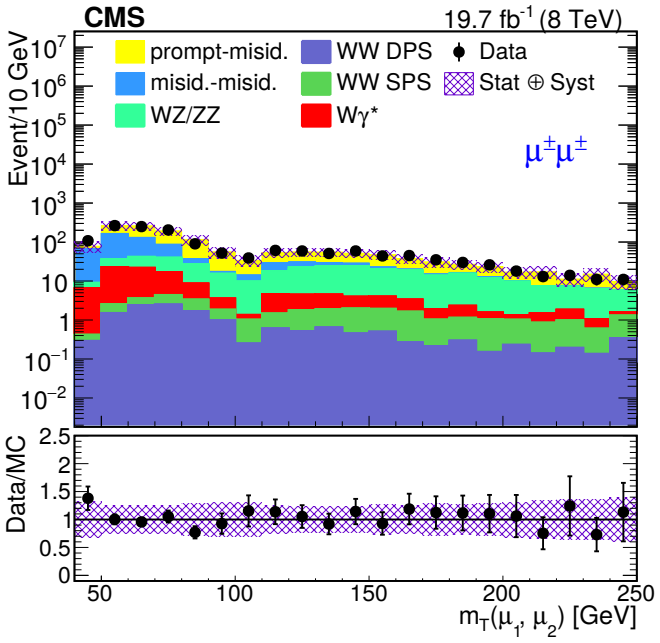

Figure 6.4: The distribution of the dimuon transverse mass, $m_T(\mu_1, \mu_2)$, for the dimuon channel. The data are represented by the black dots and the shaded histograms represent the predicted signal and background processes normalized according to the theoretical cross sections and the luminosity. The bottom panel shows the ratio of data to MC events, with associated statistical uncertainty. The hatched bands in both the panels represent the quadrature sum of statistical and systematic uncertainties.

- azimuthal angular separation between the two muons, $\Delta\phi(\vec{p}_{T_1}, \vec{p}_{T_2})$;
- transverse mass of the leading/subleading muon and $\vec{p}_T^{\,miss}$ $m_T(\mu_{1/2}, \vec{p}_T^{\,miss})$;
- dimuon transverse mass, $m_T(\mu_1, \mu_2)$;

These kinematic observables are chosen on the basis of the topology of DPS events as discussed in Section 5.10.1. Due to different background compositions for the dimuon and electron-muon final states, the optimization of input variables is done independently. Figure 6.5 shows the distributions of the kinematic observables used for the training of BDTs for the signal and background training samples. All the variables are found to have some discriminating power, are minimally correlated, and are described nicely by the data and MC predictions within systematic uncertainties.

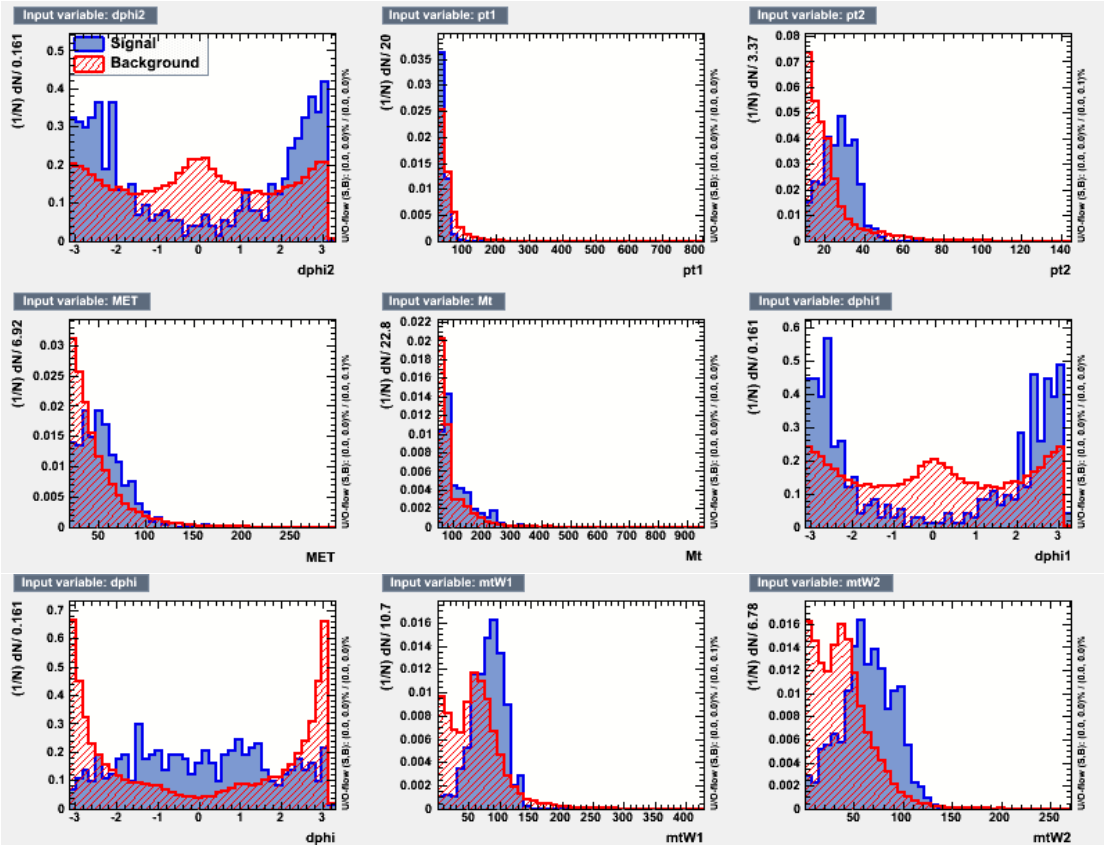

Figure 6.5: Normalized distributions of the variables used for the BDT-based analysis for the training signal and background samples.

Once the BDTs are trained, the response of the BDT discriminant is checked to ensure its reliability. In Fig. 6.6, a comparison between the BDT output for the training and testing samples is presented. The BDT output is observed to be well trained since no evidence of statistically significant discrepancy between signal and background shape is observed. Also, it is explicitly observed that the BDT discriminant has more discrimination power over any single observable. The final BDT observable is shown in Fig. 6.7, whose shape is used for the statistical analysis. The data to simulation agreement for the BDT discriminant is within systematic uncertainties.

The study of same-sign WW production via DPS in dimuon and electron-muon final states are performed to $\sigma^{\mathrm{DPS}}_{\mathrm{W^{\pm}W^{\pm}}}$ and σ_{eff}. However, 95% CL limits are placed on both of these variables due to high background rates and low signal yields. The

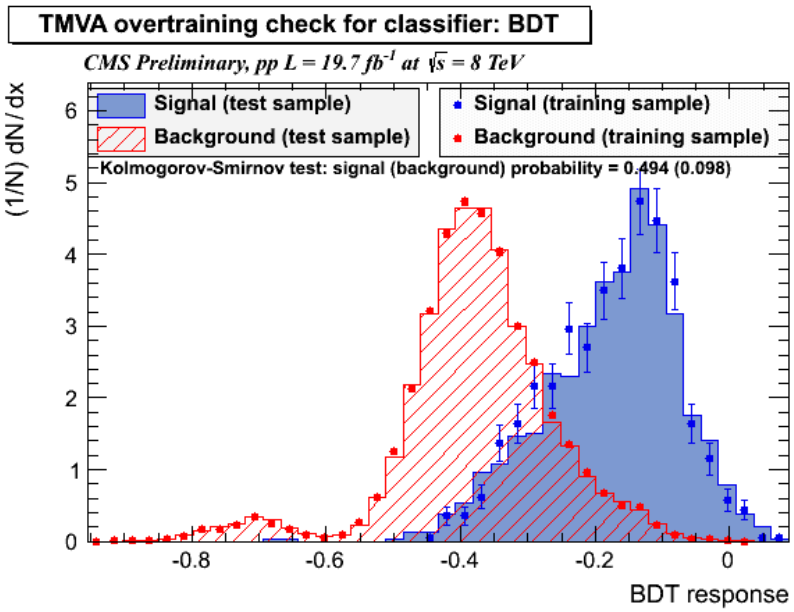

Figure 6.6: BDT response for the training and testing samples.

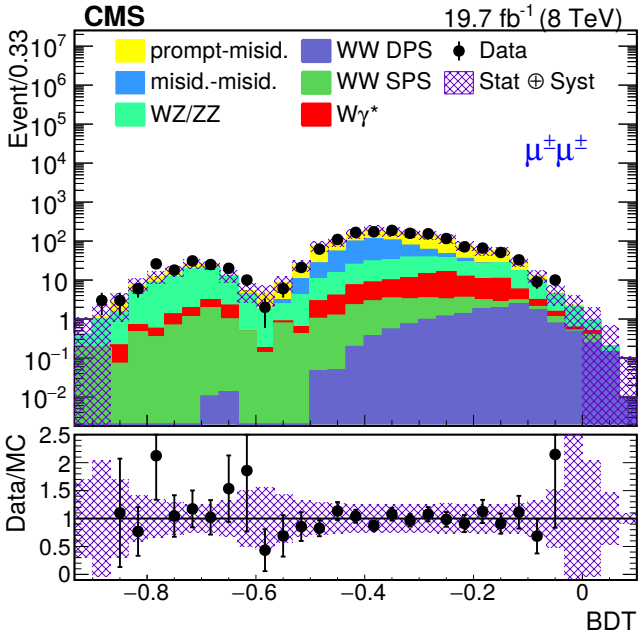

Figure 6.7: Distribution of the BDT discriminant for the dimuon channel. The data are represented by the black dots and the shaded histograms represent the predicted signal and background processes normalized according to the theoretical cross sections and the luminosity. For each individual distribution, the ratio of the number of events observed in data to that predicted by the simulation, along with the associated statistical uncertainty is also shown. The hatched bands in all cases represent the sum of the systematic and statistical uncertainties on the simulation, added in quadrature.

statistical procedure used to extract limits on the interested quantities is described in the following Section.

6.7 Combined Analysis

The main purpose of performing a statistical analysis is to obtain a quantitative measure of the likelihood that a given observation is a result of the hypothesis that the DPS signal does not exist, referred to as the background-only hypothesis, and the likelihood that it is the result of the hypothesis that the DPS signal does exist, referred to as the signal+background hypothesis. Inferences on the existence of the DPS signal might be drawn based on a comparison between these probabilities. To increase the sensitivity of analysis and to put stringent limits on the interested variables, measurements from both these final states are combined using the asymptotic approximation of the CL_s method [7, 8]. The shape of the BDT discriminant for the two final states, along with systematical and statistical uncertainties, are provided as input to the statistical analysis. A detailed description about the statistical analysis and procedure followed to set limits is described in Section 5.11.

The predicted signal and background event yields are likely to get affected by the systematic uncertainties. These effects are parametrized using a set of nuisance parameters and the predicted event yields become functions of these nuisance parameters. Using auxiliary measurements or external information, the best estimate of the value of the nuisance parameter and an estimate of its uncertainty are obtained. These pieces of information allow us to build the probability density function for the nuisance parameter. Sources of systematic uncertainties are assumed to be either fully correlated or uncorrelated among the two final states. The correlations among various systematic uncertainties across the different analyses should be properly accounted while combining the two final states. To accomplish this, the systematic uncertainties are factorized into independent sources and the systematic

uncertainties are correlated depending upon their effect and relevance towards the two final states. The systematic uncertainties arising from the theoretical predictions or from the background estimation techniques are fully correlated across the two final states, while no correlation is assumed for the statistical uncertainty. The uncertainties on the absolute scale of the integrated luminosity and pileup mismodelling are correlated across both the channels. Experimental uncertainties on the selection efficiencies, momentum scale and resolution for the muons are assumed to be correlated. The theoretical uncertainties on the production cross sections for each process are considered to be independent and these are correlated across the two final state for the relevant processes. Since the two final states use different triggers to select events, hence the systematic uncertainty on the trigger efficiency is treated as uncorrelated.

Table 6.6: Post-fit event yields with uncertainties for the background processes and the pre-fit event yields with uncertainties for the signal process. The uncertainties include both statistical and systematic components.

	Dimuon channel	Electron-muon channel
Process	Events ± syst.	Events ± syst.
WW DPS	15 ± 0.8	25 ± 1.1
WW SPS	30 ± 4.7	46 ± 1.9
WZ	266 ± 5.1	364 ± 8.5
ZZ	41 ± 1.1	80 ± 6.1
Wγ/γ^*	144 ± 7.7	1012 ± 50.8
prompt-misid.	713 ± 6.4	1894 ± 20.4
misid.-misid.	383 ± 4.7	1546 ± 12.1
Leptonic top	–	93 ± 6.4
DY	–	364 ± 27.2
WW+jets	–	32 ± 1.8
Observed	1539	5492

Table 6.7: 95% CL limit on the signal strength for the dimuon and electron-muon channels along with the combination.

95% CL	**Dimuon**	**Electron-muon**	**Combined**
Expected	2.30 pb	2.59 pb	1.66 pb
Expected $\pm1\sigma$	[0.92, 2.00] pb	[1.76, 3.90] pb	[1.14, 2.48] pb
Expected $\pm2\sigma$	[1.14, 4.98] pb	[1.27, 5.68] pb	[0.83, 3.58] pb
Observed	2.39 pb	2.21 pb	1.14 pb

Figure 6.8 shows the distributions of the BDT discriminant for the dimuon and electron-muon final states with pre-fit signal and post-fit background processes with corresponding post-fit uncertainties. Since no statistically significant excess of DPS signal events is observed, hence the pre-fit distribution of the signal is shown.

The expected and observed limits on the signal strength and cross section for inclusive WW production via DPS processes are summarized in Table 6.7 and Table 6.8, respectively. Considering a reference value for σ_{eff} of 20.7$\pm$6.6 mb as measured in W+2jets final state at 7 TeV [9] and the single-parton NNLO cross sections for $\sigma_{\text{W}^+} = 72.1\pm2.5$ nb and $\sigma_{\text{W}^-} = 50.8\pm1.9$ nb [10], $\sigma^{\text{DPS}}_{\text{W}^\pm\text{W}^\pm}$ comes out to be 0.18$\pm$0.06 pb. Figure 6.9 provides a summary of the sensitivity of the BDT-based analysis for the different final states. The expected value of $\sigma^{\text{DPS}}_{\text{W}^\pm\text{W}^\pm}$ taken from PYTHIA8 event generator is represented as a red line, while the one extracted using the factorization approach is represented using a blue line. The differences between the observed and expected limits are consistent with statistical fluctuations since the observed limits are within the green (68%) or yellow (95%) bands of the expected limit values. The observed limits for the combined analysis are stronger

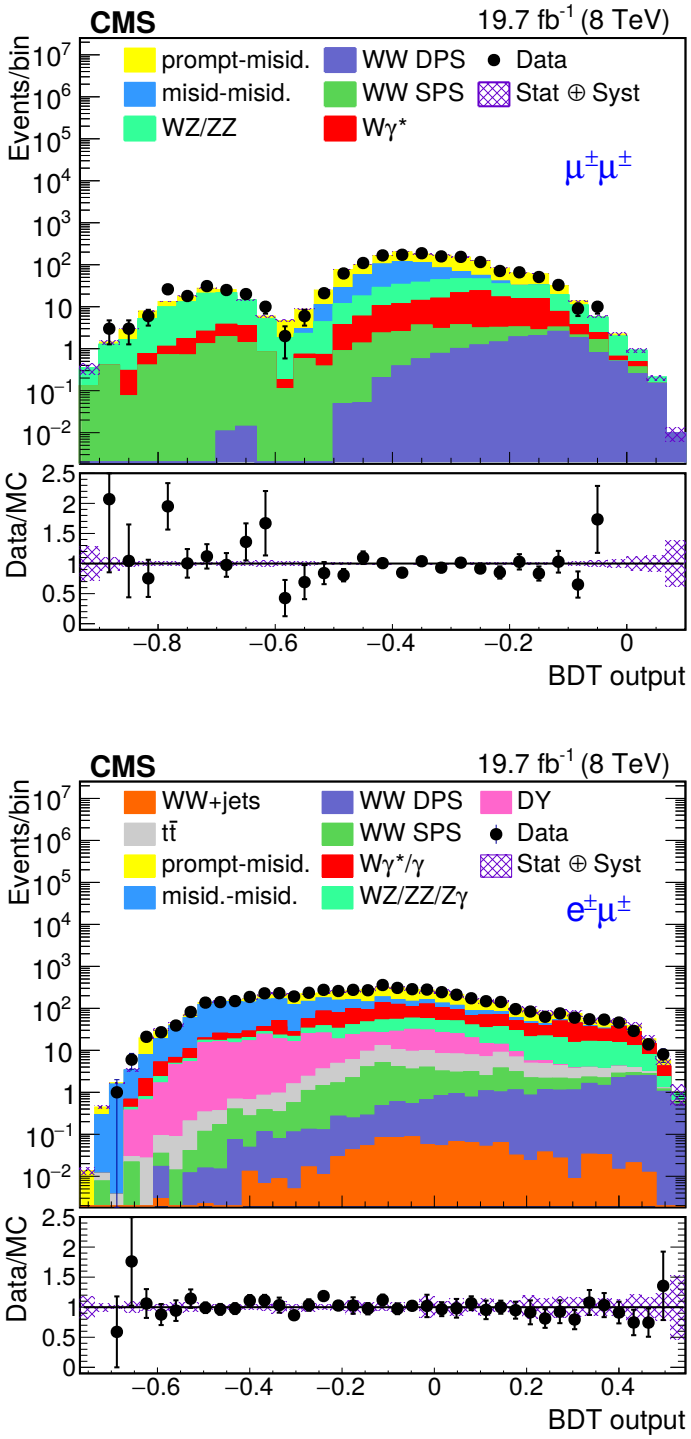

Figure 6.8: Distribution of the BDT discriminant, for the dimuon channel (top) and for the electron-muon channel (bottom). The data are represented by the black dots and the shaded histograms represent the pre-fit signal and post-fit background processes. The hatched band represents the post-fit uncertainty, which includes both the statistical and systematic components.

Table 6.8: 95% CL limit on $\sigma_{\mathrm{DPS}}^{\mathrm{W^{\pm}W^{\pm}}}$ for the dimuon and electron-muon channels along with their combination.

95% CL	**Dimuon**	**Electron-muon**	**Combined**
Expected	0.67 pb	0.78 pb	0.48 pb
Expected $\pm1\sigma$	[0.46, 1.00] pb	[0.52, 1.16] pb	[0.33, 0.72] pb
Expected $\pm2\sigma$	[0.34, 1.45] pb	[0.64, 1.71] pb	[0.24, 1.04] pb
Observed	0.72 pb	0.64 pb	0.32 pb

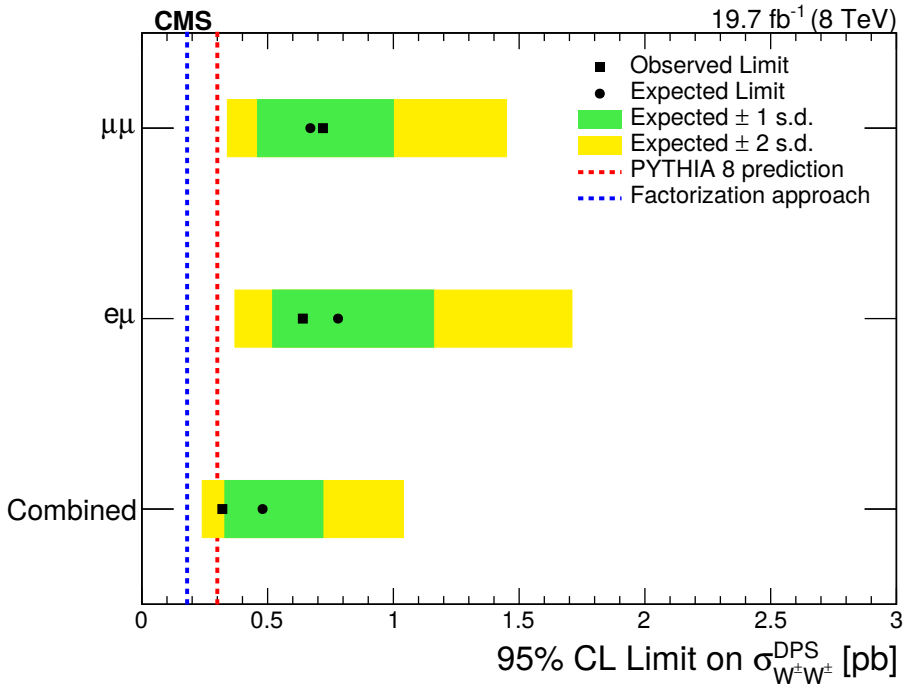

Figure 6.9: Expected and observed 95% CL upper limit on $\sigma_{\mathrm{W^{\pm}W^{\pm}}}^{\mathrm{DPS}}$ for the dimuon and electron-muon final states, along with their combination. The predicted values of $\sigma_{\mathrm{W^{\pm}W^{\pm}}}^{\mathrm{DPS}}$ from PYTHIA8 and the factorization approach are also shown.

than the limits from individual final states.

Assuming the two scatterings to be independent, a limit can be placed on σ_{eff}

using Eq. (1.6) and the SPS σ_{W^+} and σ_{W^-} cross section values at NNLO. A lower 95% CL limit on σ_{eff} can be calculated as:

$$\sigma_{\text{eff}} > \frac{\sigma^2_{W^+} + \sigma^2_{W^-}}{2 \cdot \sigma^{\text{DPS}}_{W^\pm W^\pm}} = 12.2\,\text{mb}. \tag{6.1}$$

The obtained lower limit on σ_{eff} is compared with the existing values of σ_{eff} obtained from measurements at different center-of-mass energies using a variety of processes as shown in Fig. 6.10. The combined result of the current studies is found to be compatible with the existing measurements of σ_{eff}.

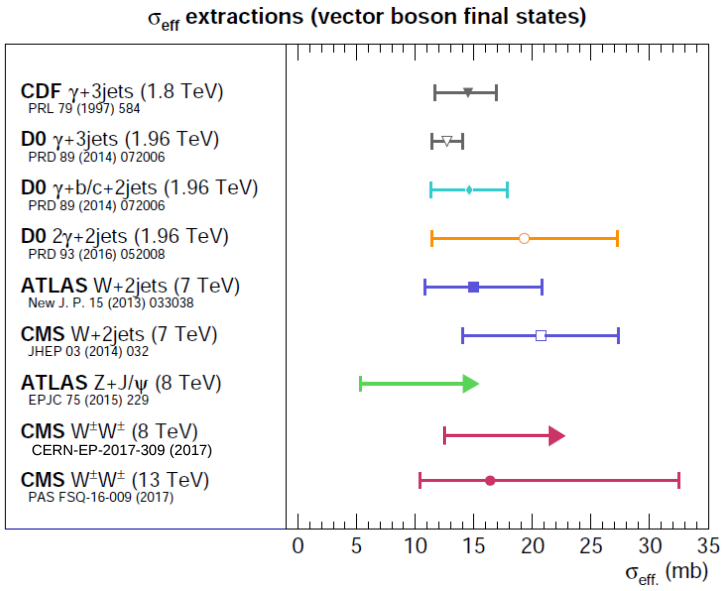

Figure 6.10: Measured values of σ_{eff} at different center-of-mass energies using different DPS processes. Different markers represent results taken from mentioned references.

6.8 Conclusions

A concise review of the study of DPS processes via same-sign WW process in the dimuon final state has been presented. The obtained results are combined with those obtained using the electron-muon final state reported in Chapter 5. The combined

studies are performed to enhance sensitivity of the analysis and to set more stringent limits on the $\sigma^{\mathrm{DPS}}_{\mathrm{W^{\pm}W^{\pm}}}$ and σ_{eff}. The limits on these quantities are improved with the combined analysis in comparison to the ones obtained from the individual final states. The extracted lower limit on the σ_{eff} is observed to be consistent with the existing measurements.

Bibliography

[1] CMS Collaboration, "Constraints on the double-parton scattering cross section from same-sign W boson pair production in proton-proton collisions at $\sqrt{s} = 8$ TeV," 2017. https://arxiv.org/abs/1712.02280.

[2] CMS Collaboration, "Double Parton Scattering cross section limit from same-sign W bosons pair production in di-muon final state at LHC," 2015. https://cds.cern.ch/record/2103756.

[3] CMS Collaboration, "Measurement of Higgs boson production and properties in the WW decay channel with leptonic final states," *JHEP*, vol. 01, p. 096, 2014. http://dx.doi.org/10.1007/JHEP01(2014)096.

[4] CMS Collaboration, "Performance of CMS muon reconstruction in *pp* collision events at $\sqrt{s} = 7$ TeV," *JHEP*, vol. 01, p. 096, 2012. http://dx.doi.org/10.1007/JHEP01(2014)096.

[5] Alekhin, Sergey and others, "The PDF4LHC Working Group Interim Report," 2011. http://cds.cern.ch/record/1318945.

[6] Hocker, Andreas and others, "TMVA - Toolkit for Multivariate Data Analysis," *CERN-OPEN-2007-007*, 2007. http://cds.cern.ch/record/1019880.

[7] Junk, Thomas, "Confidence level computation for combining searches with small statistics," *Nucl. Instrum. Meth. A*, vol. 434, p. 435, 1999. http://dx.doi.org/10.1016/S0168-9002(99)00498-2.

[8] Read, Alexander L., "Presentation of search results: The CL_s technique," *J. Phys. G*, vol. 28, p. 2693, 2002. http://dx.doi.org/10.1088/0954-3899/28/10/313.

[9] CMS Collaboration, "Study of double parton scattering using W + 2-jet events in proton-proton collisions at $\sqrt{s}$ = 7 TeV," *JHEP*, vol. 1403, p. 032, 2014. http://dx.doi.org/10.1007/JHEP03(2014)032.

[10] Gavin, Ryan and Li, Ye and Petriello, Frank and Quackenbush, Seth, "W Physics at the LHC with FEWZ 2.1," *Comput. Phys. Commun.*, vol. 184, p. 208, 2013. http://dx.doi.org/10.1016/j.cpc.2012.09.005.

[11] Particle Data Group, J. Beringer, *et al.*, "Review of particle physics," *Phys. Rev. D*, vol. 86, p. 010001, 2012. http://dx.doi.org/10.1103/PhysRevD.86.010001.